MATERIALS CHEMISTRY FRONTIERS

CHINESE CHEMICAL SOCIETY

ROYAL SOCIETY OF CHEMISTRY

RESEARCH ARTICLE

View Article Online
View Journal | View Issue

Cite this: *Mater. Chem. Front.*, 2021, **5**, 2749

An aqueous rechargeable lithium ion battery with long cycle life and overcharge self-protection†

Zhiguo Hou,[a] Lei Zhang,[a] Jianwu Chen,[a] Yali Xiong,[a] Xueqian Zhang *[a] and Yitai Qian *[b]

Received 28th December 2020,
Accepted 29th January 2021

DOI: 10.1039/d0qm01117g

rsc.li/frontiers-materials

Aqueous lithium ion batteries are receiving increasing attention for large-scale energy storage applications because of their intrinsic safety and environmental friendliness. However, they suffer from severe irreversibility issues, such as sustained water consumption, and especially low resistance to overcharging, which has rarely been studied. We find that the kinetics of H_2 evolution on the anode is much more facile than O_2 evolution on the cathode, resulting in limited resistance to overcharging. When the battery is overcharged, there is severe H_2 evolution on the anode, triggering O_2 evolution. The structure collapse of the anode, resulting from oxidation by O_2, leads to rapid capacity fading. Here, Zn^{2+} is added into the electrolyte to solve these problems without any loss of battery energy density. When charged in the end, the Zn^{2+} will be reduced to Zn metal exhibiting high over potential for H_2 evolution, which can suppress H_2 evolution. A $LiMn_2O_4/NaTi_2(PO_4)_3$ full cell exhibits enhanced overcharging performance and excellent cycling stability up to 10 000 cycles at 10C.

Introduction

The ever-increasing demand for electricity leads to a large amount of carbon dioxide emission, which causes a greenhouse effect exacerbating global warming.[1] Thus, electricity obtained from renewable power sources (such as solar power, wind turbines, tide energy, and geothermal energy) are promising because of their sustainability, environmental friendliness, and wide distribution.[2] There is an increasing need for large-scale energy storage systems (ESSs).[3] Batteries possessing a number of desirable characteristics such as high energy efficiency, long cycle life, pollution-free operation, controllable scale to meet different grid situations, and low maintenance costs, have been considered as prospective candidates for power sources for large-scale ESS applications.[4–7] However, the intermittent performance of the renewable power sources sometimes outputs excess energy that exceeds that which the battery is able to withstand. For example, the voltage output of wind turbines is unstable, which poses a challenge for the battery to tolerate over-charging.[8] The most common rechargeable battery systems are lithium ion batteries (LIBs), which show the highest energy density and longest cycle life among various commercial rechargeable batteries. However, some intrinsic characteristics, such as their safety and cost, mean that their adoption in EES has been slower.[1,3,9] Aqueous rechargeable lithium ion batteries (ARLIBs) are promising alternatives for large-scale applications which could resolve these concerns: (i) the aqueous electrolyte has intrinsic safety, (ii) the battery can be manufactured in air, and (iii) the battery is easy to recycle.[10–13]

Dahn *et al.* first reported ARLIBs, using a $LiMn_2O_4$ (LMO) cathode and a VO_2 anode in 1994, with a working potential of 1.5 V and energy density of 90 W h kg^{-1} (based on total mass of both the cathode and anode).[14] The Xia group developed an ARLIB, using a $LiFePO_4$ cathode and $LiTi_2(PO_4)_3$ anode, with a working potential of 0.9 V, exhibiting an energy density of 50 W h kg^{-1} and up to 1000 cycle life.[15] However, the narrow electrochemical stability window (1.23 V) of aqueous electrolyte sets an intrinsic limit on the practical voltage and energy output of ARLIBs.[16,17] In particular, the narrow electrochemical stability window makes the ARLIBs less tolerant to overcharging. Wang *et al.* reported a "water-in-salt" electrolyte with an expanded electrochemical stability window of 3.0 V.[16] A series of ARLIBs using such electrolyte composed of different electrochemical couples demonstrated high working voltage and energy at nearly 100% coulombic efficiency.[9,18–24] However, the high concentration electrolyte exhibiting relatively low ion conductivity and high viscosity will decrease the rate capability and raise cost problems in practical applications. It has been demonstrated that the slightly higher voltage of 1.5 V can be realized in existing aqueous battery chemistries due to the

[a] *Jiangsu University of Technology, ZhongWu Road 1801, 213001, Changzhou, China. E-mail: xueqian@mail.ustc.edu.cn*
[b] *School of Chemistry and Materials, University of Science and Technology of China, Jinzhai Road 96, 130012, Hefei, China*

† Electronic supplementary information (ESI) available. See DOI: 10.1039/d0qm01117g

kinetic overpotentials of H_2 or O_2 evolutions.[25–27] And there is a general knowledge that the kinetics of H_2 evolution are much more facile than O_2 evolution. This is the so-called cathodic challenge, in which the most severe challenge for ARLIBs comes from the stabilization of the anode rather than the cathode surface.[25,28,29] When overcharged, the battery suffers from serious H_2 evolution, which induces severe irreversibility issues, such as battery bulge, sustained water consumption and capacity fading.

In this work, we found that H_2 evolution on the $NaTi_2(PO_4)_3$ (NTP) anode results in the electrolyte pH increasing, which triggers O_2 evolution on the LMO cathode. O_2 diffused to the anode reacts with NTP lead to the structure collapse. The H_2 is electrochemically passivated and is hard to be oxidized and accumulated in the battery, resulting in battery bulge and water consumption. The structure collapse of NTP causes irreversible battery capacity fading. Zn^{2+} has similar reduction potential to NTP. When overcharged, the Zn^{2+} will be reduced to Zn metal exhibiting high over potential for H_2 evolution, which can suppress H_2 evolution. Therefore, Zn^{2+} was added into electrolyte to solve these problems. A rechargeable aqueous battery based on an LMO cathode and NTP anode delivered stability over 10 000 cycles with energy density of 100 W h kg^{-1}. And the battery can tolerate over-charging to 2.15 V with little water decomposition and good capacity retention.

Results and discussion

The LMO was synthesized by solid state reaction. Its crystal structure was evaluated by X-ray diffraction (XRD). As shown in Fig. 1a, all the peaks in the XRD patterns of LMO are indexed as a single phase spinel with a cubic structure. The sharp diffraction peaks at 18.7°, 36.34°, 37.93°, 44.1°, 48.37°, 58.35°, 64.17°, 76.0°, 76.8° and 45.7° can be assigned to the (015), (0012), (107), (0114), and (110) planes with a space group of $Fd\bar{3}m$ (JCPDS No.: 18-0736), respectively. Particle morphology observed by scanning electron microscope (SEM) is shown in Fig. 1b. Secondary particles of spherical shape *ca.* 5 μm in diameter are agglomerates of *ca.* 500 nm primary particles. It can be seen that primary particles composed of nanosized particles stack together with planar-lamination shape with a particle size of 400–600 nm. The transmission electron microscope (TEM) shows the well-defined crystallinity of the (111) plane (Fig. 1c and d). The NTP was produced by a sol–gel method. The XRD peaks for the NTP can be indexed in the rhombohedral crystal system with a space group *R3c* (JCPDS No.:85-2265) without any obvious impurities (Fig. 1e). The morphology of NTP is agglomerates composed of individual particles with narrow size distribution in the range of 200–300 nm (Fig. 1f). The TEM images in Fig. 1g illustrate the presence of a thin carbon layer about 3–6 nm thick on the surface of the NTP particles. It can also be seen that the lattice fringes are well defined within the particle (Fig. 1h). The interplanar space is about 0.37 nm, which should be ascribed to the (113) crystal face. The thermogravimetric analysis (TG) curve for the NTP recorded in air shows that the carbon content is proportional to the weight loss between 300 and 800 °C. The amount of coated carbon was calculated to be around 3 wt% (Fig. S1, ESI†). Before being tested in an aqueous electrolyte, the electrochemical performances of LMO and NTP were measured in an organic electrolyte. As shown in Fig. S2 (ESI†), the initial charge capacity of LMO is about 110 mA h g^{-1} and the initial discharge capacity is about 105 mA h g^{-1} at 0.1C (1C = 110 mA h g^{-1} for the cathode). The NTP exhibits an initial sodium ion storage discharge capacity of about 120 mA h g^{-1} and charge capacity of 115 mA h g^{-1} at 0.1C (1C = 133 mA h g^{-1} for anode), which is very close to its theoretical capacity.

The cyclic voltammograms (CV) of the as-prepared LMO cathode and NTP anode in 1 M Li_2SO_4 + 1 M Na_2SO_4 aqueous electrolyte (1–1 electrolyte) were carried out using a three

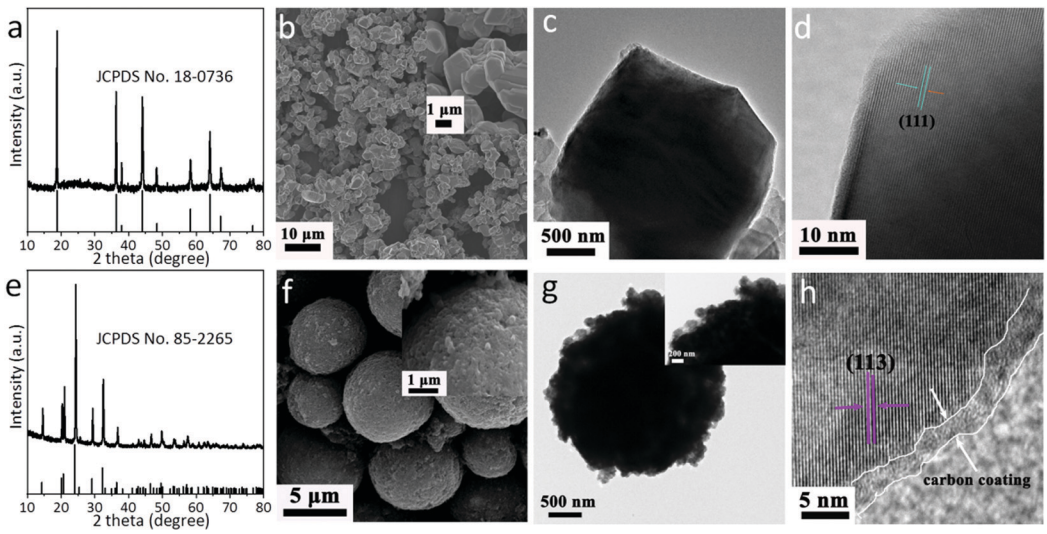

Fig. 1 Characterization of pristine LMO and NTP materials. (a) XRD pattern of pristine LMO powder. (b) SEM image of LMO. (c and d) TEM and HR-TEM images of LMO. (e) XRD pattern of pristine NTP powder. (f) SEM image of NTP. (g and h) TEM and HR-TEM images of NTP.

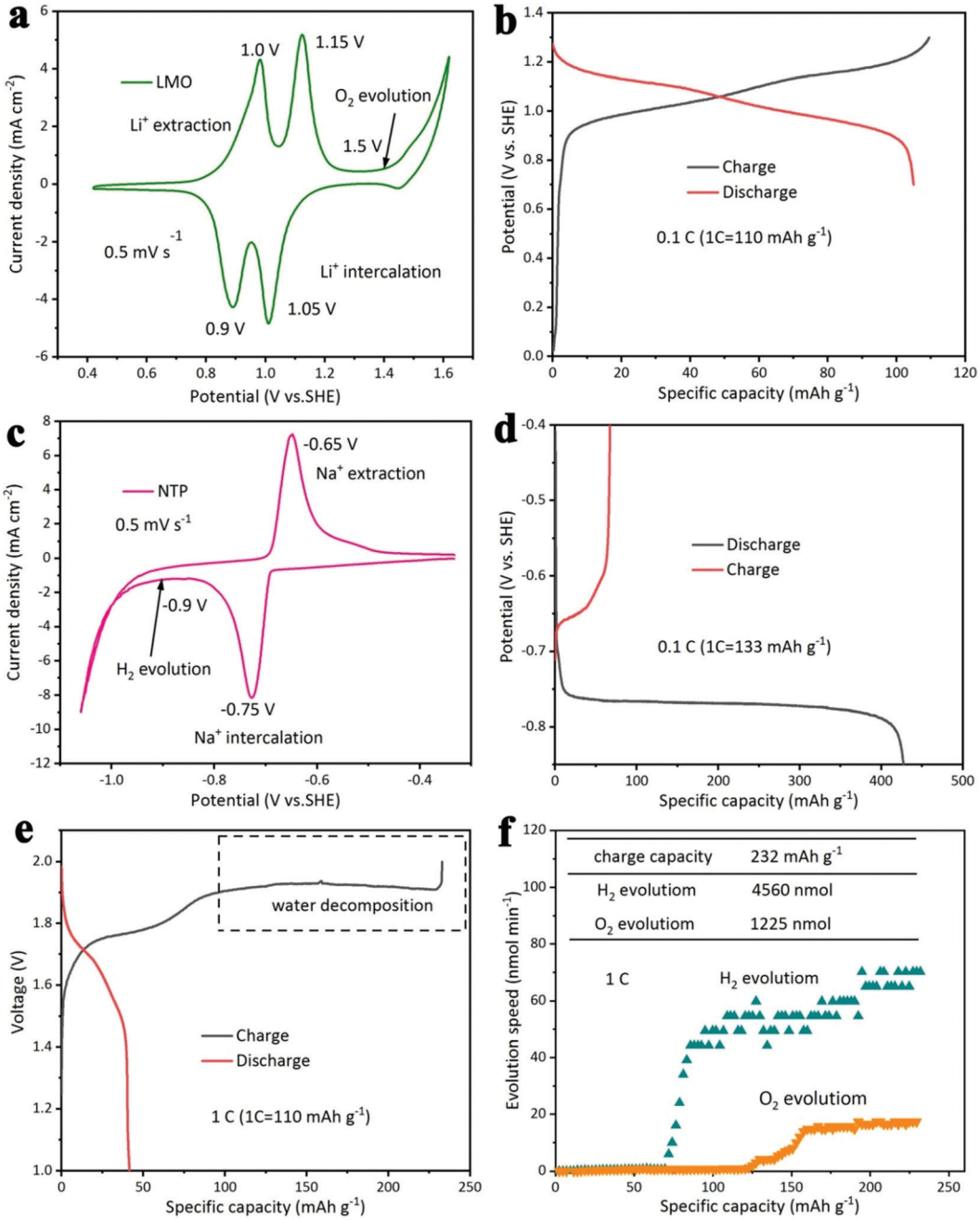

Fig. 2 Electrochemical performances for LMO and NTP materials in 1–1 electrolyte. (a) CV results of the LMO cathode using a three electrode system at a scan rate of 0.5 mV s^{-1}. (b) Charge/discharge profiles of the LMO cathode using a three electrode system at 0.1C. (c) CV results of the NTP anode using a three electrode system at a scan rate of 0.5 mV s^{-1}. (d) Galvanostatic discharge–charge curves of the NTP anode using a three electrode system at 0.1C. (e) Charge/discharge profiles of the LMO/NTP full cell at 1C in 1–1 electrolyte among 1.0 and 2.0 V. (f) H_2 and O_2 evolution monitored during the first charging process of the LMO/NTP full cell at 1C until 2.0 V using DEMS.

electrode system, in which Pt was used as a counter electrode and the AgCl/Ag electrode was used as a reference electrode. All of the working potentials have been converted to standard hydrogen electrode (SHE) reference for convenience. The Na_2SO_4 added in electrolyte can decrease the cost. From the CV results in Fig. 2a, two pairs of redox peaks, located at 1.0 and 1.15 V oxidation potential *vs.* SHE, are observed for LMO, which agrees with the insertion/extraction reaction in the organic electrolyte.[30] It also shows that it is possible to fully extract a Li ion from the hosts before 1.2 V. The O_2 evolution occurred at about 1.5 V *vs.* SHE, which is much higher than 1.2 V. This gives a big buffer for the cathode to be overcharged. As shown in Fig. 2b, the initial charge capacity of LMO at 0.1C is about 110 mA h g^{-1} with a charge cut-off potential of 1.3 V *vs.* SHE. And the initial discharge capacity is about 105 mA h g^{-1}, exhibiting a high initial coulombic efficiency of 95%. After 1000 cycles at 1C rate, the LMO delivers a

high capacity retention of 95% (Fig. S3, ESI†). This suggests that the LMO shows good reversibility and the influence of O_2 evolution is negligible. The CV result of NTP shows that one pair of redox peaks are located at about −0.75 (reduction peak) and −0.65 V (oxidation peak) *vs.* SHE (Fig. 2c). It also shows that it is possible for NTP to fully insert two Na ions into the hosts before −0.85 V. However, the H_2 evolution occurred at about −0.9 V *vs.* SHE. As shown in Fig. 2d, The discharge capacity is 420 mA h g^{-1}, which is much more than its theoretical capacity. The initial charge capacity is only 80 mA h g^{-1}, suggesting that the discharge of NTP is overwhelmed by serious H_2 evolution. This indicates that H_2 evolution should easily happen accompanied by Na ion intercalation into NTP, especially at the end of charging. After 100 cycles at 1C, the capacity retention of NTP is merely 15% (Fig. S4, ESI†).

A full cell was assembled with a LMO cathode and NTP anode with a mass ratio of 1.1 : 1 using a 1–1 electrolyte. The typical charge/discharge profiles of the full cell at 1C (1C = 110 mA h g^{-1} base on cathode) between 1 and 2 V are shown in Fig. 2e. The battery only exhibits one characteristic plateau at ~1.72 V and delivers a charging capacity of about 60 mA h g^{-1}. The second characteristic charge plateau of the full cell is overwhelmed by a water decomposition process. The total charging capacity is about 232 mA h g^{-1}, which is much higher than the theoretical capacity. To further study this phenomenon, differential electrochemical mass spectrometry (DEMS) was used to monitor the gaseous compounds during the initial charging process, which is an effective method to quantitatively study this decomposition process.[31] As shown in Fig. 2f, the water splitting cumulatively produces 4560 nmol H_2 and 1225 nmol O_2 continuously. There is distinct H_2 evolution when the cell is charged above 1.8 V, which suggests that H_2 evolution is accompanying the NTP reduction reaction especially at the end of charging. It should be noted that after the battery is overcharged until the capacity reached 120 mA h g^{-1}, the O_2 evolution is started. And the amounts of H_2 and O_2 do not precisely obey the 2 : 1 stoichiometric ratio. We suppose that the H_2 evolution on the anode results in a pH increase of the electrolyte, which will trigger O_2 evolution. The corresponding decomposition of water is about 82 μg. The amount of electrolyte in the battery is about 100 μL, which suggests that almost all water is decomposed. This should result in serious polarization of the battery. As observed in Fig. 2f, there emerges a voltage jump at the end of charging, which should be ascribed to the serious polarization of the battery at the end of the charging process. As shown in Fig. S5 (ESI†), the pH of the electrolyte is increased to 13, after the battery is overcharged until the capacity reached 120 mA h g^{-1}. The increased pH induces O_2 evolution. As shown in Fig. S6 (ESI†), the O_2 evolution occurred at about 1.2 V *vs.* SHE in a 1–1 electrolyte with a pH of 13. This indicates that at the end of charging, the O_2 evolution should overwhelm the Li ion extraction process. The initial discharge capacity is only 40 mA h g^{-1}. The irreversible capacity loss for an initial cycle is too big. After 10 cycles at 1C, the battery only exhibits 10% capacity retention, which indicates the serious water decomposition (Fig. S7, ESI†). The cycling performances of the LMO/NTP full cell using 1 M Li_2SO_4 electrolyte were also measured at 1C among 1.0 and 2.0 V (Fig. S8, ESI†). The initial charging capacity is about 320 mA h g^{-1}, which is much higher than its theoretical capacity. The initial discharging capacity is only 42 mA h g^{-1}. After 10 cycles at 1C, the battery only exhibits 12% capacity retention. It has been demonstrated that all negative electrode materials suitable for ARLIBs react with water and O_2.[15]

The XRD test of an NTP anode after 10 cycles was carried out. As shown in Fig. 3a, the typical diffraction peak of NTP is weakened. However, there emerge diffraction peaks ascribed to TiO_2, which suggests that the NTP is decomposed. The O_2 generated on the cathode diffuses to the anode and reacted with the anode, leading to NTP structure collapse ($0.5O_2 + Na_3Ti_2(PO_4)_3 + 3H_2O \rightarrow 2TiO_2 + 3H_2PO4^- + 3Na^+$). The TEM image shows that the surface of the NTP particles is fragmentary, and the lattice fringes become irregular (Fig. 3b). What's more, the carbon coating also seems to be damaged (Fig. 3c). The carbon coating should be oxidized by O_2 ($C + O_2 + 2OH^- \rightarrow CO_3^{2-} + H_2O$). The electrochemical impedance spectroscopy (EIS) results show that the electron conductivity and ion conductivity of NTP are decreased after cycling (Fig. S9, ESI†). It can be concluded that the O_2 leads to NTP structure collapse which causes irreversible capacity fading.

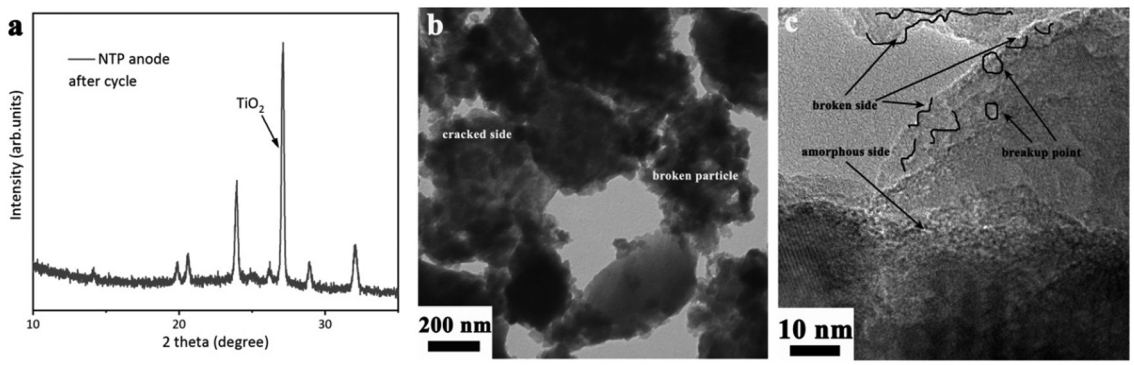

Fig. 3 Characterization of the NTP material in the fully charged state after 10 cycles in 1–1 electrolyte. (a) XRD of the NTP anode after cycling. (b and c) TEM and HR-TEM images of the NTP particles after cycling.

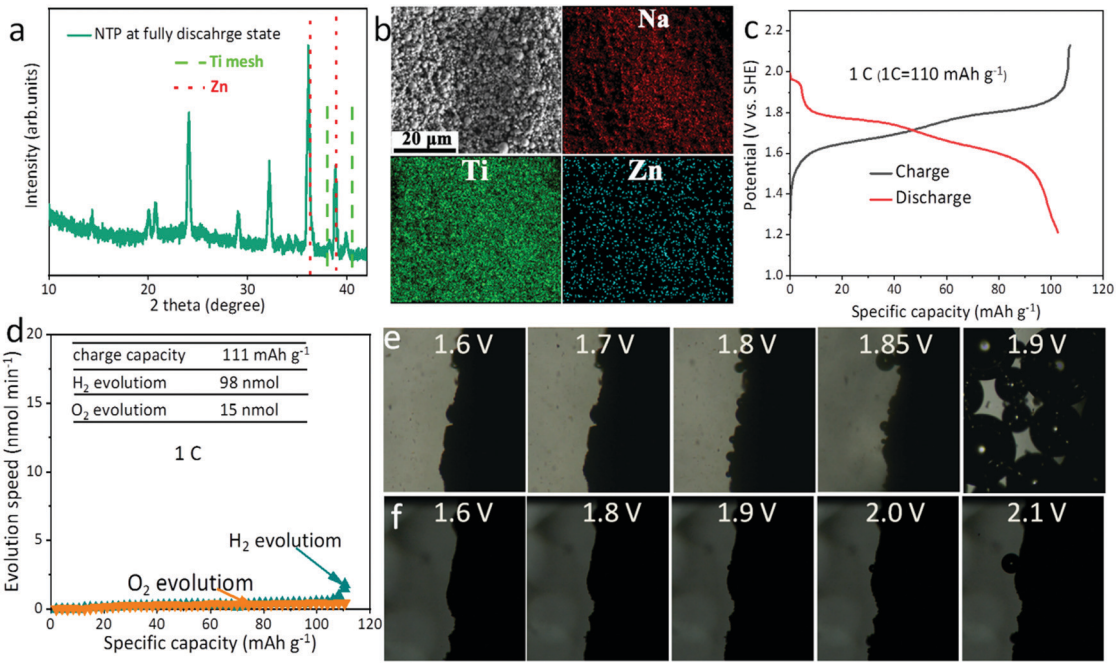

Fig. 4 Characterization of the NTP anode and electrochemical performances of the full cell in a 1–1 electrolyte with 0.1 M Zn^{2+} addition. (a) XRD of the NTP anode at the fully discharged state. (b) SEM image and EDS mapping images of the NTP anode after cycling at the fully discharged state. (c) Charge/discharge profiles of the LMO/NTP full cell at 1C among 1.2 and 2.15 V. (d) H_2 and O_2 evolution monitored during the first charging process of the LMO/NTP full cell at 1C until 2.15 V using DEMS. *In situ* optical microscope images of the front surfaces of (e) the LMO/NTP full cell using 1–1 electrolyte at 1C among 1.2 and 2.15 V, and (f) the LMO/NTP full cell in a 1–1 electrolyte with 0.1 M Zn^{2+} addition at 1C among 1.2 and 2.15 V.

The key point is to suppress the H_2 evolution. As we all know, the redox potential of Zn^{2+} is about −0.78 V *vs.* SHE, which is very similar to the NTP. Zn metal exhibits high kinetic overpotential of H_2 evolution. What's more, the addition of Zn^{2+} will not decrease the specific capacity of the LMO/NTP battery.[32–34] Therefore, Zn^{2+} was added into the electrolyte. As shown in Fig. S10 (ESI†), there emerges a typical oxidation peak located at about −0.75 V *vs.* SHE of a 1–1 electrolyte added with 0.1 M $ZnSO_4$, which should be ascribed to Zn. It should be noted that the H_2 evolution potential is pushed to about −1.1 V *vs.* SHE, which is much lower than −0.85 V. This gives a big buffer to avoid H_2 evolution when the battery is overcharged. To demonstrate the presence of Zn, XRD of the NTP anode after a discharging process was tested. As shown in Fig. 4a, there are typical diffraction peaks of Zn metal. The energy dispersive spectroscopy (EDS) elemental mapping images (Fig. 4b) indicate the homogeneous distribution of elements Ti, and Zn in the selected region, suggesting the even reduction of Zn on the anode surfaces.

The full cell based on an LMO cathode and an NTP anode using the 1–1 electrolyte added with 0.1 M $ZnSO_4$ was assembled. The battery was cycled between 1.2 and 2.15 V at a current rate of 1C with an anode and cathode material mass ratio of 1.1 : 1. As shown in Fig. 4c, there are two charging platforms located at about 1.72 and 1.85 V. Even as the battery is charged to 2.15 V, there is no obvious water decomposition. The charging capacity is about 111 mA h g^{-1}, which is close to its capacity exhibited in an organic electrolyte. After the full charging process of the full cell, the Zn^{2+} will be reduced to Zn on the NTP anode. According to Inductive Coupled Plasma Emission Spectrometer-Atomic Emission Spectroscopy (ICP-AES) tests, the weight fraction of Zn of the NTP anode is about 1.21% (Table S1, ESI†). The initial discharging curve of the battery delivers a high capacity of 105 mA h g^{-1} with three definite platforms at 1.9, 1.76 and 1.6 V, respectively. The discharge plateau located at 1.9 V should be attributed to oxidation of Zn. The discharge capacity at 1.9 V is about 10 mA h g^{-1}. The next two platforms should belong to oxidation of NTP. The irreversible capacity caused by LMO and NTP should be 6 mA h g^{-1}, which is common in ARLIB systems.[15,16] The addition of Zn does not decrease the discharge capacity, but compensates part of this irreversible capacity loss caused by NTP. The total irreversible capacity loss for the initial cycle is only 6 mA h g^{-1}, suggesting the high reversibility of the full cell. To quantitatively study this rapid decrease in the irreversible capacity, DEMS was carried out. As shown in Fig. 4d, the O_2 evolution is almost eliminated during the whole charging process. There is very little amount (98 nmol) of H_2 detected. Only when the battery is charged to 2.15 V, there is a little H_2 detected. This suggests that the reduced Zn on the anode effectively suppresses the H_2 evolution reaction. To further demonstrate the suppression of water decomposition and lack of Zn dendrite growth during a charging process, an optical microscope equipped with a digital camera was used for *in situ* monitoring of the NTP anode in a transparent LMO/NTP full cell in different electrolytes. The battery was charged at 1 C rate. The optical microscopy images of the LMO/NTP full cell in a 1-1 electrolyte show that when it is charged to 1.8 V, small bubbles

arise (Fig. 4e). When it is charged to 1.85 V, there are obvious big bubbles on the anode surface. When the battery is charged to 1.9 V, the transparent LMO/NTP full cell is full of bubbles. In contrast, there are no obvious bubbles when the LMO/NTP full cell is charged to 2.0 V using a 1–1 electrolyte with 0.1 M Zn^{2+} addition (Fig. 4f). When it is charged to 2.1 V, there emerge little bubbles. And there is no obvious Zn dendrite growth on the anode during the charging process. The *in situ* optical microscope images are consistent with the DEMS results, which demonstrate the effectively suppressed H_2 evolution reaction. The extensive water decomposition faced in a traditional electrolyte is remarkably inhibited.

The amount of Zn^{2+} addition plays an important role, which is worth discussing in detail. As we all know, there is dendrite growth during Zn^{2+} repeated plating/stripping processes.[35–39] If there is too much Zn^{2+}, the LMO/NTP battery may suffer from this thorny issue. As shown in Figure S11, after 20 cycles in a 1–1 electrolyte with 0.2 M Zn^{2+}, the battery suffers from short circuiting. The SEM image of the NTP anode after short circuiting shows that there are many dendrites unevenly distributed through the surface of the anode (Fig. S12, ESI†). In contrast, after 100 cycles at 1C in 1–1 electrolyte with 0.1 M Zn^{2+}, the SEM image from the side view of the NTP electrode shows that there is no sign of dendrites after the discharging process (Fig. S13, ESI†). The inhibition of H_2 evolution may be incomplete if the Zn^{2+} addition is too small. As shown in Fig. S14 (ESI†), the H_2 evolution potential is about −0.95 V *vs.* SHE in a 1–1 electrolyte with 0.05 M Zn^{2+}, which is only a little lower than −0.85 V. The initial discharge capacity of the NTP anode is 240 mA h g^{-1}, suggesting that the H_2 evolution is accompanied by a reduction reaction of NTP (as shown in Fig. S15, ESI†). Therefore, a 1–1 electrolyte added with 0.1 M $ZnSO_4$ should be optimal.

The electrochemical performances of the LMO/NTP battery were systematically examined in a 1–1 electrolyte added with 0.1 M $ZnSO_4$. Fig. 5a presents the electrochemical window of this ARLB. The cut-off charge voltage can be extended to 2.15 V at 0.1C. The over-charging voltage is about 0.15 V, which is very high for an aqueous battery.[29] The galvanostatic charge/discharge curves of LMO show that there are two distinct plateaus located at 1.0 and 1.15 V *vs.* SHE, attributed to the redox reactions of LMO. The initial charge/discharge capacity is about 110 and 105 mA h g^{-1}, respectively. The initial coulombic efficiency is about 95%. The discharge/charge profiles of NTP show that there is a flat plateau located at −0.75 V *vs.* SHE, which should be ascribed to the Na ion intercalation into NTP. No obvious H_2 evolution is observed until the NTP anode is discharged to −1.0 V *vs.* SHE. The discharge capacity of the plateau located at −0.75 V *vs.* SHE is about 130 mA h g^{-1}, which is about 10 mA h g^{-1} more than that obtained in an organic electrolyte. It should be ascribed to the reduction of Zn^{2+}. The initial charge capacity is about 125 mA h g^{-1}, which is higher than that obtained in organic capacity. This should be ascribed to the oxidation of Zn. In the charging/discharging curves for the full cell, there are two evident plateaus located at about 1.75 and 1.6 V, indicating clearly the redox reactions of LMO and NTP. No obvious H_2 evolution is observed until the battery is fully charged to 2.15 V. There is a small discharge platform located at 1.9 V, which should be the redox reactions of LMO and Zn. The initial charge/discharge capacity is about 111 and 105 mA h g^{-1}, respectively, suggesting a high initial coulombic efficiency of 94%. As shown in Fig. 5b, after the initial charging/discharging process, the coulombic efficiency is quickly increased to about 99.5% at 1C. This suggests that due to the very little amount of H_2 evolution, the battery

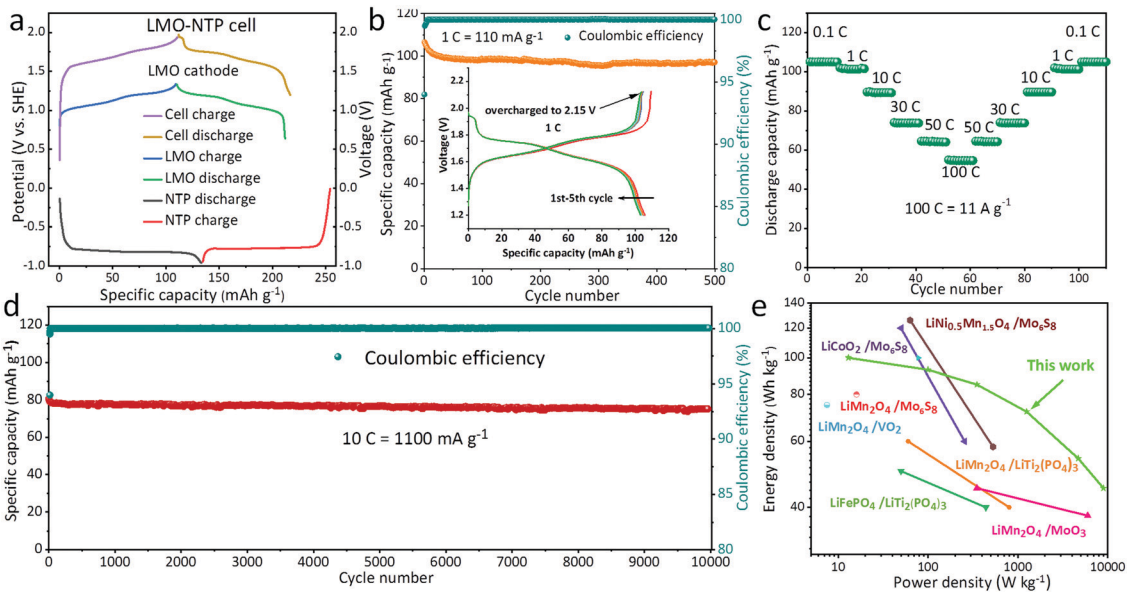

Fig. 5 Electrochemical performances for LMO and NTP materials in a 1–1 electrolyte with 0.1 M Zn^{2+} addition. (a) Charge and discharge curves of the NTP anode, the LMO cathode and the full cell consisting of the two electrodes at 0.1C. (b) Cycling stability and coulombic efficiency of the full cell when it is overcharged to 2.15 V at 1C. (c) Rate-capability of the full cell among 1.2 and 2.15 V. (d) Long cycle performances of the full cell at 10C among 1.2 and 2.15 V. (e) Ragone plots showing a comprehensive comparison of the energy density and power density with reported results.

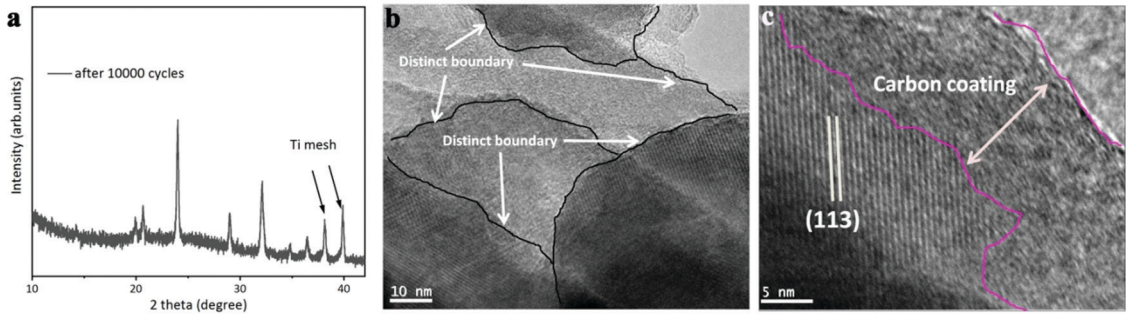

Fig. 6 Characterization of the NTP material at the fully charged state after 10 000 cycles in 1–1 electrolyte with Zn^{2+} addition. (a) XRD of the NTP anode after cycling. (b and c) TEM and HR-TEM images of NTP particles at the fully charged state after cycling.

exhibits high coulombic efficiency. After 500 cycles at 1C, the LMO/NTP battery delivers a high capacity retention of 86% after 500 cycles at 1C, which suggests the good cycling stability. As shown in Fig. 5c, the battery exhibits high rate capability. Even at a very high rate of 100C, the battery still delivers a high discharge capacity of 55 mA h g^{-1}. Fig. 5d shows the long cycling performance of the battery between 1.2 and 2.15 V at 10C. The battery exhibits 10% capacity loss after 10 000 cycles at 10C with nearly 100% coulombic efficiency under extreme cycling conditions without relaxation between cycles. As shown in gravimetric Ragone plots in Fig. 5e and computational details in the supporting information, both high energy and power densities (100 W h kg^{-1} at 13 W kg^{-1}, and 45 W h kg^{-1} at 8973 W kg^{-1}) can be simultaneously achieved based on the total mass of active materials. On the basis of a comprehensive summary (as compared in Fig. 5e and summarized in Table S2, ESI†), to the best of our knowledge, this is so far the highest rate-capability and the longest cycle life among various reported ARLIBs. All of the above results show that the battery exhibits a significant improvement in cycling stability and rate capability. The above results demonstrated that the battery exhibits a good overcharging self-protection even when it is overcharged to 2.15 V. So far, there are no literature reports that are published to deal with this problem in aqueous batteries.

As demonstrated above, by adding Zn^{2+} into the electrolyte, an aqueous battery with good cycling ability, rate capability and over-charging self-protection has been practically demonstrated. The morphology and structure of NTP were analyzed by TEM and XRD. As shown in Fig. 6a, there are no obvious impurity peaks except for NTP after 10 000 charge/discharge cycles in the 1–1 electrolyte with Zn^{2+} additive. Fig. 6b show the surface morphology of the NTP anode. A ~5 nm thick conformal coating layer is observed on an NTP particle. The HRTEM image (Fig. 6c) further reveals the amorphous nature of the surface coating layer which should be attributed to the carbon coating. In contrast with Fig. 3b, no evident surface defects were observed on the NTP particles that were now protected by the carbon coating. The NTP retains the original well-crystalline structure after the 10 000 charge/discharge cycles, as demonstrated by the XRD and HR-TEM results. The EIS results show that the electron conductivity and ion conductivity of NTP after the 10 000 charge/discharge cycles are similar to the original electrode (shown in Fig. S16, ESI†). Thus the good structure stability of the NTP anode and the inhibited water decomposition contribute to the long cycle life of the battery.

Conclusions

We have demonstrated that due to the kinetics of H_2 evolution being much more facile than O_2 evolution, there occurs severe H_2 evolution on the NTP anode accompanied by the Na intercalation process. This leads to the electrolyte pH increasing, which triggers O_2 evolution. The NTP anode is oxidized by O_2 resulting in its structure collapse, which leads to irreversible capacity loss. By adding Zn^{2+} into the electrolyte, the Zn^{2+} can be reduced to Zn metal at the end of the charging process. The Zn reduced on the anode exhibits high over potential for H_2 evolution, which can effectively suppress H_2 evolution. A rechargeable aqueous battery based on the LMO cathode and NTP anode is assembled and delivers high stability over 10 000 cycles with an energy density of 100 W h kg^{-1}. Even when it is overcharged to 2.15 V, the battery still retains good cycling stability with little H_2 evolution. What's more, this overcharge protection strategy is simple without any loss of energy density. In terms of its high safety, long cycling life, high power, low cost and low toxicity, the LMO/NTP aqueous rechargeable battery should be a very suitable energy storage and conversion device for large-scale stationary power sources that store energy from sustainable sources, such as wind and solar power.

Author contributions

Zhiguo Hou, Xueqian Zhang and Lei Zhang synthesized the samples and assembled the batteries; Lei Zhang, Jiawu Chen and Yali Xiong contributed to the analysis. Xueqian Zhang and Zhiguo Hou wrote the paper. All authors contributed to the general discussion. Yitai Qian checked the paper and polished the article to improve the quality of the article.

Conflicts of interest

There are no conflicts to declare.

Acknowledgements

This work was financially supported by the National Key Research and Development Program of China (2016YFB0901503), Jiangsu Province Natural Science Research of Universities (19KJB150025), National Natural Science Foundation of China (21875238 and 21831006), and Jiangsu Province Innovative and Entrepreneurial Doctor Project (No. KYQ19021 and KYQ19019).

Notes and references

1 M. Armand and J.-M. Tarascon, Building better batteries, *Nature*, 2008, **451**, 652–657.
2 D. Bin, F. Wang, A. G. Tamirat, L. Suo, Y. Wang, C. Wang and Y. Xia, Progress in aqueous rechargeable sodium-ion batteries, *Adv. Energy Mater.*, 2018, **8**, 1703008.
3 H. Kim, J. Hong, K.-Y. Park, H. Kim, S.-W. Kim and K. Kang, Aqueous rechargeable Li and Na ion batteries, *Chem. Rev.*, 2014, **114**, 11788–11827.
4 P. J. Hall and E. J. Bain, Energy-storage technologies and electricity generation, *Energy Policy*, 2008, **36**, 4352–4355.
5 B. Dunn, H. Kamath and J.-M. Tarascon, Electrical energy storage for the grid: A battery of choices, *Science*, 2011, **334**, 928–935.
6 M. H. Lee, S. J. Kim, D. Chang, J. Kim, S. Moon, K. Oh, K.-Y. Park, W. M. Seong, H. Park and G. Kwon, Toward a low-cost high-voltage sodium aqueous rechargeable battery, *Mater. Today*, 2019, **29**, 16–35.
7 D. Larcher and J. Tarascon, Towards greener and more sustainable batteries for electrical energy storage, *Nat. Chem.*, 2014, **7**, 19–29.
8 E. Hittinger, T. Wiley, J. Kluza and J. Whitacre, Evaluating the value of batteries in microgrid electricity systems using an improved energy systems model, *Energy Convers. Manage.*, 2015, **89**, 458–472.
9 C. Yang, J. Chen, X. Ji, T. P. Pollard, X. Lü, C.-J. Sun, S. Hou, Q. Liu, C. Liu and T. Qing, Aqueous Li-ion battery enabled by halogen conversion–intercalation chemistry in graphite, *Nature*, 2019, **569**, 245–250.
10 Y. Wang, J. Yi and Y. Xia, Recent progress in aqueous lithium-ion batteries, *Adv. Energy Mater.*, 2012, **2**, 830–840.
11 J. Whitacre, T. Wiley, S. Shanbhag, Y. Wenzhuo, A. Mohamed, S. Chun, E. Weber, D. Blackwood, E. Lynch-Bell and J. Gulakowski, An aqueous electrolyte sodium ion functional large format energy storage device for stationary applications, *J. Power Sources*, 2012, **213**, 255–264.
12 W. Tang, Y. Zhu, Y. Hou, L. Liu, Y. Wu, K. P. Loh, H. Zhang and K. Zhu, Aqueous rechargeable lithium batteries as an energy storage system of superfast charging, *Energy Environ. Sci.*, 2013, **6**, 2093–2104.
13 Z. Guo, Y. Zhao, Y. Ding, X. Dong, L. Chen, J. Cao, C. Wang, Y. Xia, H. Peng and Y. Wang, Multi-functional flexible aqueous sodium-ion batteries with high safety, *Chem*, 2017, **3**, 348–362.
14 W. Li, J. Dahn and D. Wainwright, Rechargeable lithium batteries with aqueous electrolytes, *Science*, 1994, **264**, 1115–1118.
15 J.-Y. Luo, W.-J. Cui, P. He and Y.-Y. Xia, Raising the cycling stability of aqueous lithium-ion batteries by eliminating oxygen in the electrolyte, *Nat. Chem.*, 2010, **2**, 760–765.
16 L. Suo, O. Borodin, T. Gao, M. Olguin, J. Ho, X. Fan, C. Luo, C. Wang and K. Xu, "Water-in-salt" electrolyte enables high-voltage aqueous lithium-ion chemistries, *Science*, 2015, **350**, 938–943.
17 Y. Yamada, K. Usui, K. Sodeyama, S. Ko, Y. Tateyama and A. Yamada, Hydrate-melt electrolytes for high-energy-density aqueous batteries, *Nat. Energy*, 2016, **1**, 16129–16137.
18 L. Suo, O. Borodin, W. Sun, X. Fan, C. Yang, F. Wang, T. Gao, Z. Ma, M. Schroeder, A. von Cresce, S. M. Russell, M. Armand, A. Angell, K. Xu and C. Wang, Advanced high-voltage aqueous lithium-ion battery enabled by "water-in-bisalt" electrolyte, *Angew. Chem., Int. Ed.*, 2016, **55**, 7136–7141.
19 F. Wang, Y. Lin, L. Suo, X. Fan, T. Gao, C. Yang, F. Han, Y. Qi, K. Xu and C. Wang, Stabilizing high voltage $LiCoO_2$ cathode in aqueous electrolyte with interphase-forming additive, *Energy Environ. Sci.*, 2016, **9**, 3666–3673.
20 F. Wang, L. Suo, Y. Liang, C. Yang, F. Han, T. Gao, W. Sun and C. Wang, Spinel $LiNi_{0.5}Mn_{1.5}O_4$ cathode for high-energy aqueous lithium-ion batteries, *Adv. Energy Mater.*, 2016, **7**, 1600922.
21 L. Suo, O. Borodin, Y. Wang, X. Rong, W. Sun, X. Fan, S. Xu, M. A. Schroeder, A. V. Cresce and F. Wang, "Water-in-salt" electrolyte makes aqueous sodium-ion battery safe, green, and long-lasting, *Adv. Energy Mater.*, 2017, **7**, 1701189.
22 C. Yang, J. Chen, T. Qing, X. Fan, W. Sun, A. von Cresce, M. S. Ding, O. Borodin, J. Vatamanu and M. A. Schroeder, 4.0 V aqueous Li-ion batteries, *Joule*, 2017, **1**, 122–132.
23 C. Yang, X. Ji, X. Fan, T. Gao, L. Suo, F. Wang, W. Sun, J. Chen, L. Chen, F. Han, L. Miao, K. Xu, K. Gerasopoulos and C. Wang, Flexible aqueous Li-ion battery with high energy and power densities, *Adv. Mater.*, 2017, **29**, 1701972.
24 F. Wang, O. Borodin, M. S. Ding, M. Gobet, J. Vatamanu, X. Fan, T. Gao, N. Eidson, Y. Liang and W. Sun, Hybrid aqueous/non-aqueous electrolyte for safe and high-energy Li-ion batteries, *Joule*, 2018, **2**, 927–937.
25 J. Y. Luo and Y. Y. Xia, Aqueous lithium-ion battery $LiTi_2(PO_4)_3/LiMn_2O_4$ with high power and energy densities as well as superior cycling stability, *Adv. Funct. Mater.*, 2007, **17**, 3877–3884.
26 W. Tang, L. Liu, Y. Zhu, H. Sun, Y. Wu and K. Zhu, An aqueous rechargeable lithium battery of excellent rate capability based on a nanocomposite of MoO_3 coated with ppy and $LiMn_2O_4$, *Energy Environ. Sci.*, 2012, **5**, 6909–6913.
27 S. Liu, S. H. Ye, C. Z. Li, G. L. Pan and X. P. Gao, Rechargeable aqueous Lithium-ion battery of $TiO_2/LiMn_2O_4$ with a high voltage, *J. Electrochem. Soc.*, 2011, **158**, A1490–A1497.
28 Y. Wang, X. Cui, Y. Zhang, L. Zhang, X. Gong and G. Zheng, Achieving high aqueous energy storage *via* hydrogen-generation passivation, *Adv. Mater.*, 2016, **28**, 7626–7632.
29 K. Xu and C. Wang, Batteries: Widening voltage windows, *Nat. Energy*, 2016, **1**, 16161.

30 W. Tang, Y. Hou, F. Wang, L. Liu, Y. Wu and K. Zhu, $LiMn_2O_4$ nanotube as cathode material of second-level charge capability for aqueous rechargeable batteries, *Nano Lett.*, 2013, **13**, 2036–2040.

31 L. Suo, D. Oh, Y. Lin, Z. Zhuo, O. Borodin, T. Gao, F. Wang, A. Kushima, Z. Wang and H.-C. Kim, How solid-electrolyte interphase forms in aqueous electrolytes, *J. Am. Chem. Soc.*, 2017, **139**, 18670–18680.

32 R. Wei, X. Wang, B. Xi, Z. Feng, H. Li, W. Chen, Y. Jia, J. Feng and S. Xiong, Layer-by-layer stacked $(NH_4)_2V_4O_{9\cdot0.5}H_2O$ nanosheet assemblies with intercalation pseudocapacitance for high rate aqueous zinc ion storage, *ACS Appl. Energy Mater.*, 2020, **3**, 5343–5352.

33 W. Wang, T. Wang, X. Fan, C. Zhang, J. Hu, H. Chen, Z. Fang and J. Yan, Freeze-drying-assisted synthesis of mesoporous CoMoO4 nanosheets as anode electrode material for enhanced lithium batteries, *Chem. Res. Chin. Univ.*, 2019, **35**, 261–270.

34 X. Ji and H. Jiang, A perspective: the technical barriers of Zn metal batteries, *Chem. Res. Chin. Univ.*, 2020, **36**, 55–60.

35 F. Wang, O. Borodin, T. Gao, X. L. Fan, W. Sun, F. D. Han, A. Faraone, J. A. Dura, K. Xu and C. S. Wang, Highly reversible zinc metal anode for aqueous batteries, *Nat. Mater.*, 2018, **17**, 543–550.

36 V. Yufit, F. Tariq, D. S. Eastwood, M. Biton, B. Wu, P. D. Lee and N. P. Brandon, Operando visualization and multi-scale tomography studies of dendrite formation and dissolution in zinc batteries, *Joule*, 2019, **3**, 485–502.

37 J. F. Parker, C. N. Chervin, I. R. Pala, M. Machler, M. F. Burz, J. W. Long and D. R. Rolison, Rechargeable Nickel–3d Zinc batteries: An energy-dense, safer alternative to lithium-ion, *Science*, 2017, **356**, 415–418.

38 J. Zheng, J. Yin, D. Zhang, G. Li, D. C. Bock, T. Tang, Q. Zhao, X. Liu, A. Warren and Y. Deng, Spontaneous and field-induced crystallographic reorientation of metal electrodeposits at battery anodes, *Sci. Adv.*, 2020, **6**, eabb1122.

39 J. Zheng, Q. Zhao, T. Tang, J. Yin, C. D. Quilty, G. D. Renderos, X. Liu, Y. Deng, L. Wang and D. C. Bock, Reversible epitaxial electrodeposition of metals in battery anodes, *Science*, 2019, **366**, 645–648.